

# Sn@C Evolution from Yolk-shell to Core-shell in Carbon Nanofibers with Suppressed Degradation of Lithium Storage

## Abstract

Metallic Sn has high conductivity and high theoretical capacity for lithium storage but it suffers from severe volume change in lithiation/delithiation leading to capacity fade. Yolk-shell and core-shell Sn@C spheres interconnected by carbon nanofibers were synthesized by thermal vapor and thermal melting of electrospun nanofibers to improve the cycling stability. Sn particles in yolk-shell spheres undergo dynamic structure evolution during thermal melting to form core-shell spheres. The core-shell spheres linked along the carbon nanofibers show outstanding performance and are better than the yolk-shell system for lithium storage, with a high capacity retention of 91.8% after 1000 cycles at 1 A g<sup>-1</sup>. The superior structure of core-shell spheres interconnected by carbon nanofibers has facile electron conductivity and short lithium ion diffusion pathways through the carbon nanofibers and shells, and re-develops Sn@C structures with Sn clusters embedded into carbon matrix during electrochemical cycling, enabling the high performance.

Keywords: tin; yolk-shell; core-shell; nanofiber; lithium storage

## Introduction

Lithium-ion batteries (LIBs) are the most popular energy storage devices to store/release electricity in portable electronics, and are now penetrating the market in electric vehicles and grid-scale energy storage because of their superior energy and power density performance compared to other rechargeable systems. New materials are sought to improve the energy density of LIBs and/or optimize the power, charging rate, cost, lifespan, safety and environmental impact<sup>1</sup>. Current LIB technology is based on insertion-compound electrodes and graphite has dominated as an anode material since 1991<sup>2</sup>. With a low operating voltage, approaching that of the Li/Li<sup>+</sup> couple, graphite has a gravimetric capacity of 372 mAh g<sup>-1</sup> and volumetric capacity of 850 mAh cm<sup>-3</sup> when the lithium-inserted compound, LiC<sub>6</sub> is formed. Developers require systems that outperform the graphite anode for the next-generation of LIBs with high-energy density<sup>3,4</sup>.

Metallic tin (Sn) has attracted great interest as a promising alternative to graphite as the anode in LIBs because Sn has a large theoretical specific capacity (992 mAh g<sup>-1</sup>) and volumetric capacity (2020 mAh cm<sup>-3</sup>) which arises by forming an alloy of Li<sub>4.4</sub>Sn. Further, its electrical resistivity of  $1.1 \times 10^{-7} \Omega \cdot \text{m}$  at room temperature is nearly an order of magnitude lower than that of graphite<sup>5-7</sup>. The operation potential of Sn is around 0~0.4 V, slightly higher than metallic Li, minimizing the risk of safety related to dendrite formation<sup>8</sup>. Sn is also less toxic and less expensive than other potential candidate materials<sup>9</sup>. However, the huge volume change of ~300% for Sn, upon lithiation/de-lithiation causes pulverization and delamination of Sn active materials from current collectors, leading to severe capacity fade and poor cycle life of batteries incorporating Sn anodes.

Production of Sn materials at the nanoscale has been employed to address the large volume variation of Sn in the electrochemical reaction with lithium ions. Nanostructured Sn is capable of

alleviating the volume change and facilitating  $\text{Li}^+$ /electron transport by increasing surface area-to-volume ratios and decreasing diffusion lengths<sup>5</sup>. Moreover, Sn-based nanostructures have been incorporated in anchored, layered-sandwich, core-shell and porous structures to further relieve the volume expansion/contraction problem and increase the packing density and energy/power density. Zhang<sup>10</sup> *et al.* have reported that pitaya-like Sn@C nanocomposites with ultrasmall particles of 8 nm prepared by an aerosol spray pyrolysis method, alleviates the problems associated with the volume change of Sn on repeated lithiation/de-lithiation. Xu<sup>11</sup> *et al.* used the same method to prepare a uniform nano-Sn/C composite for lithium storage in which the carbon matrix offered mechanical support and prevented agglomeration upon cycling. Yu<sup>12, 13</sup> *et al.* have encapsulated Sn nanoparticles into porous multichannel carbon microtubes and coaxial nanofibers using carbonization of electrospun nanofibers. Liu<sup>14</sup> *et al.* also used an electrospinning and pyrolysis method to homogeneously encapsulate ultrasmall Sn nanodots into porous N-doped carbon nanofibers to yield a material that showed good cyclability in sodium-ion batteries. Zhang<sup>15</sup> *et al.* reported a yolk-shell Sn@C nanobox composite in which the thickness of the carbon nanobox can be controlled. They concluded that the thickness of the carbon shell has a substantial influence on the electrochemical performance in terms of specific capacity and cycling stability.

In this work, yolk-shell and core-shell Sn@C spherical nanostructures are prepared by a thermal vapor mechanism and thermal fusion of Sn; the as-formed spheres are interconnected along the carbon nanofibers. These carbon nanofibers provide high electron conduction network for these spheres, of which the yolk-shell spheres have nano fragments of Sn in the shell, while core-shell spheres have intact Sn blocks. The dynamics of the Sn-C structure evolution on thermal melting were characterized by electron microscopy. It is found that the core-shell Sn@C

outperforms the yolk-shell structures for lithium storage, and shows much better long-term cycling stability than published results due to the improved shell properties and re-established Sn@C structures during electrochemical cycling.

## Results and discussion

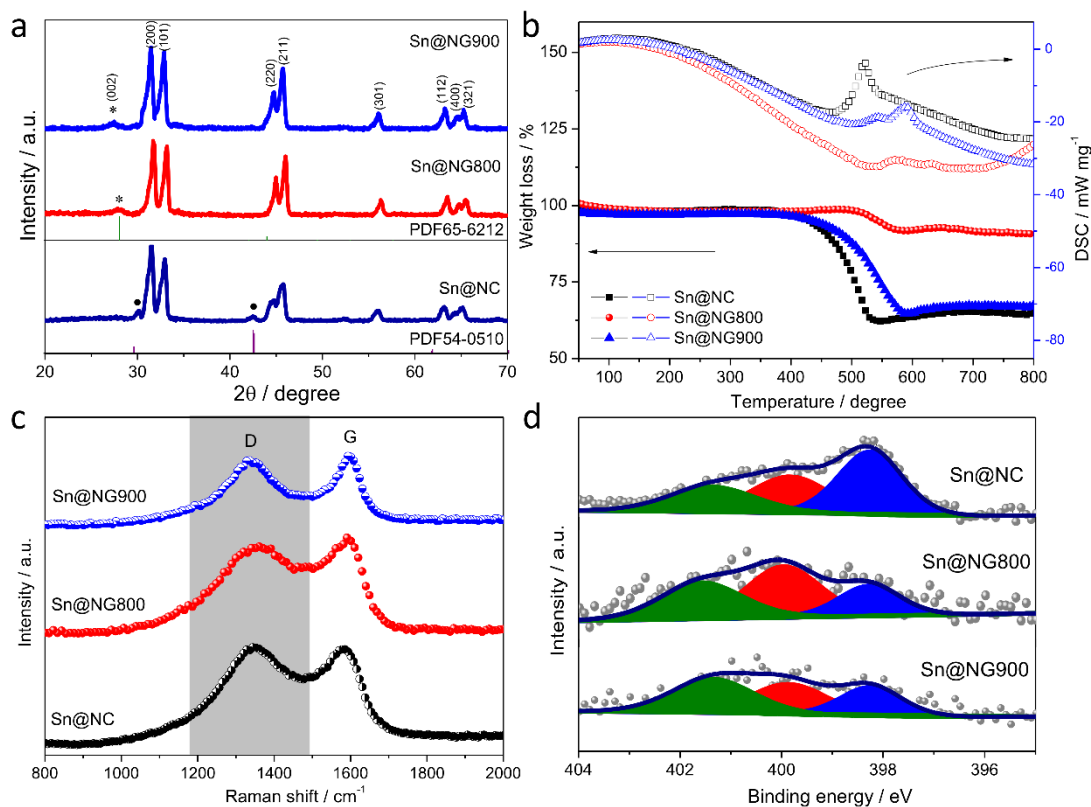


Figure 1 Material characterization of the as-prepared Sn@NC, Sn@NG800 and Sn@NG900. (a) XRD patterns. The dots denote the patterns of carbon and the stars signify graphite. (b) TGA/DSC curves. (c) Raman spectra. (d) High-resolution N1s XPS with three de-convolution peaks.

Yolk-shell and core-shell Sn@C spheres interconnected with carbon nanofibers are prepared by pyrolysis of the ZnSn(OH)<sub>6</sub> cubes-incorporated electrospun fibers. The precursor ZnSn(OH)<sub>6</sub>

cubes are synthesized according to a reported solvothermal method<sup>16</sup>, scanning electron microscopy (SEM) images and X-ray diffraction (XRD) patterns of the as-prepared material are displayed in Figure S1. The cubes mixed with polyacrylonitrile (PAN) at a weight ratio of 1:1 are dispersed in dimethylformamide (DMF) to form a uniform gel which is used to form nanofibers by an electrospinning method. The resultant matrix consists of cubes wrapped by the polymer shells and interconnected along the PAN fibers, as shown in Figure S2. The fibers obtained are then sintered in an Ar atmosphere at high temperatures to evaporate Zn via a thermal vapor mechanism<sup>17</sup> and pyrolyze PAN into conductive nitrogen-doped carbon (NC)<sup>18</sup>. XRD patterns in Figure 1a indicate that the sample annealed at 800 °C for 2 h contains Sn (PDF No. 65-7657) and tetragonal carbon (PDF No. 54-0501). The black dots denote the characteristic peaks of the crystalline carbon and the sample is labelled as Sn@NC. Extending the pyrolysis time to 5 h at 800 °C, or increasing temperature to 900 °C for 2 h, promotes the graphitization of PAN and forms nitrogen-doped graphite (NG) through the cyclization of the PAN<sup>19</sup>. Figure 1a displays the typical (002) plane of graphite (PDF No. 65-6212) denoted with an asterisks at ~27°, which is consistent with the reported result<sup>20</sup>. However, the low intensity and broad shape of the (002) diffraction peak suggest low graphitization and crystallization, as well as the existence of disordered structures<sup>21-24</sup>. The samples obtained following 800 and 900 °C pyrolysis for 5h and 2h are labelled as Sn@NG800 and Sn@NG900, respectively. To understand the pyrolyzed products of PAN, the PAN fibers without ZnSn(OH)<sub>6</sub> cubes were sintered in Ar at 800 °C for 2 h and 5 h respectively, to form the carbon materials, namely PAN-2h and PAN-5h. SEM images and XRD patterns of PAN-2h and PAN-5h are shown in Figure S3. Both samples display similar nanosized diameter but micronmeter length for the fibers and the existence of low graphitization graphite. Distinguished from the graphite-like structure of PAN-2h, the NC in Sn@NC does not

have the graphite-like features resulting from the thermal dispersion of Zn evaporation in a short heating time of 2h. The (002) layer distance of the NC and NG shells are 0.296 and 0.32 nm, according to Bragg's Law, and the mean sizes of the crystal Sn domains along (200) in Sn@NC, Sn@NG800 and Sn@NG900 are 17.2, 18 and 17.6 nm respectively, based on the Scherrer equation,  $\tau = K\lambda/\beta\cos\theta$ , where  $\tau$  is the mean size of the crystalline domains,  $K$  a dimensionless shape factor with a typical value of 0.9,  $\lambda$  the radiation wavelength,  $\beta$  full width at half maximum intensity in radians and  $\theta$  the Bragg angle. The increase in both layer spacing and domain size results from the annealing conditions which can enhance graphitization and crystal growth.

Simultaneous Thermogravimetry and Differential Scanning Calorimetry (TGA/DSC) curves in Figure 1b, indicate higher thermal stability of NG than NC, as revealed by the increase of the burning point in the TGA measurement: Sn@NC 521 °C, Sn@NG800 584 °C and Sn@NG900 592 °C. The weight loss of the three samples at the burning temperatures is due to the depletion of carbon and incompletely-pyrolyzed polymer residues left post pyrolysis, which is 36.1% for Sn@NC, 6.7% for Sn@NG800 and 33.7% for Sn@NG900. In the TGA measurement, Sn is also oxidized by the reaction  $C + Sn + 2O_2 \rightarrow SnO_2 + CO_2$ . The mass difference between the starting Sn/C composite and the resulting SnO<sub>2</sub> yields carbon contents in Sn@NC, Sn@NG800 and Sn@NG900 of 49.7%, 26.5% and 47.8% respectively. Raman spectra of the NC and NG materials are displayed in Figure 1c. Two broad bands located at 1336–1361 and 1585–1593 cm<sup>-1</sup> are assignable to the disordered band (D) and graphitic band (G). The D band results from the out-of-plane vibrations of sp<sup>2</sup> carbon, caused by structural disorders and defects which lower the crystalline symmetry of the quasi-infinite lattice. The G band is related to the first-order scattering of the in-plane stretching vibration mode (E<sub>2g</sub>) of sp<sup>2</sup> carbons<sup>25</sup>. The intensity ratios of

D to G bands ( $I_D/I_G$ ), directly proportional to the amount of turbostratic disorder of carbons are 1.02, 0.96 and 0.99, for Sn@NC, Sn@NG800 and Sn@NG900, respectively. The low  $I_D/I_G$  ratio of Sn@NG800 implies a higher graphitization degree than Sn@NG900 than Sn@NC, although the strong D band indicates a large amount of defects in the structure. The nitrogen content of the samples are measured by X-ray photoelectron spectroscopy (XPS) and the results shown in Table S1 and Figure S4 indicate that the surface ratios of N of Sn@NC, Sn@NG800 and Sn@NG900 are 5.53%, 2.64% and 1.9%. It appears the increased temperature and graphitization reduce the nitrogen content of the graphitic carbon, in agreement with previously published results<sup>26</sup>. The large content of N in Sn@NC causes a downshift of the G band ( $1585\text{ cm}^{-1}$ ) in the Raman spectra compared with Sn@NG800 ( $1591\text{ cm}^{-1}$ ) and Sn@NG900 ( $1593\text{ cm}^{-1}$ ), as a result of the  $\pi$ - $p^*$  conjunction in the formation of the N-C bonds<sup>25</sup>. The high quantity of nitrogen in the incompletely-pyrolyzed PAN may increase the  $I_D/I_G$  ratio. Figure 1d plots the deconvoluted high-resolution N 1s XPS peaks with pyridinic N ( $C\equiv N$  at 398.2 eV), pyrrolic N ( $C=N$  at 399.9 eV), and graphitic or quaternary N ( $C-N$  at 401.6 eV) as the chemical entities<sup>27-29</sup>, the atomic structures of which are displayed in Figure S5. The chemical bonding between carbon and nitrogen enhances the interaction of the carbons with adsorbents, leaving the carbon framework more chemically active<sup>30</sup>. The pyridinic N (N5) and pyrrolic N (N6) moieties are capable of enhancing capacity by reversibly binding with charge carriers and exhibiting fast kinetics, compared with the more inert graphitic N<sup>27</sup>. The quantities of the three moieties in the samples are listed in Table 1. The high ratio of pyridinic N in Sn@NC may arise from the incompletely-decomposed PAN in which N atoms are chemically bonded to carbon. The increase in the pyrolysis temperature and time leads to a decrease in pyridinic N but increase in both pyrrolic and graphitic N. The specific surface areas of three samples are evaluated by nitrogen

adsorption/desorption at 77 K, and isotherms are plotted in Figure S6. Brunauer–Emmett–Teller (BET) surface areas of Sn@NC, Sn@NG800 and Sn@NG900 are 14.4, 85.9 and 30 m<sup>2</sup> g<sup>-1</sup>. The pore size distributions from the Density Functional Theory (DFT) are similar for all samples, predominantly below 6 nm in diameter. However, the cumulative pore volume of Sn@NG800, 0.077 cm<sup>3</sup> g<sup>-1</sup> is much larger than Sn@NC (0.024 cm<sup>3</sup> g<sup>-1</sup>), and Sn@NG90 (0.029 cm<sup>3</sup> g<sup>-1</sup>). The higher surface area and pore volume of Sn@NG800 in comparison with the other two, denotes the more completed pyrolysis of PAN owing to the extended processing time, consistent with the above analysis.

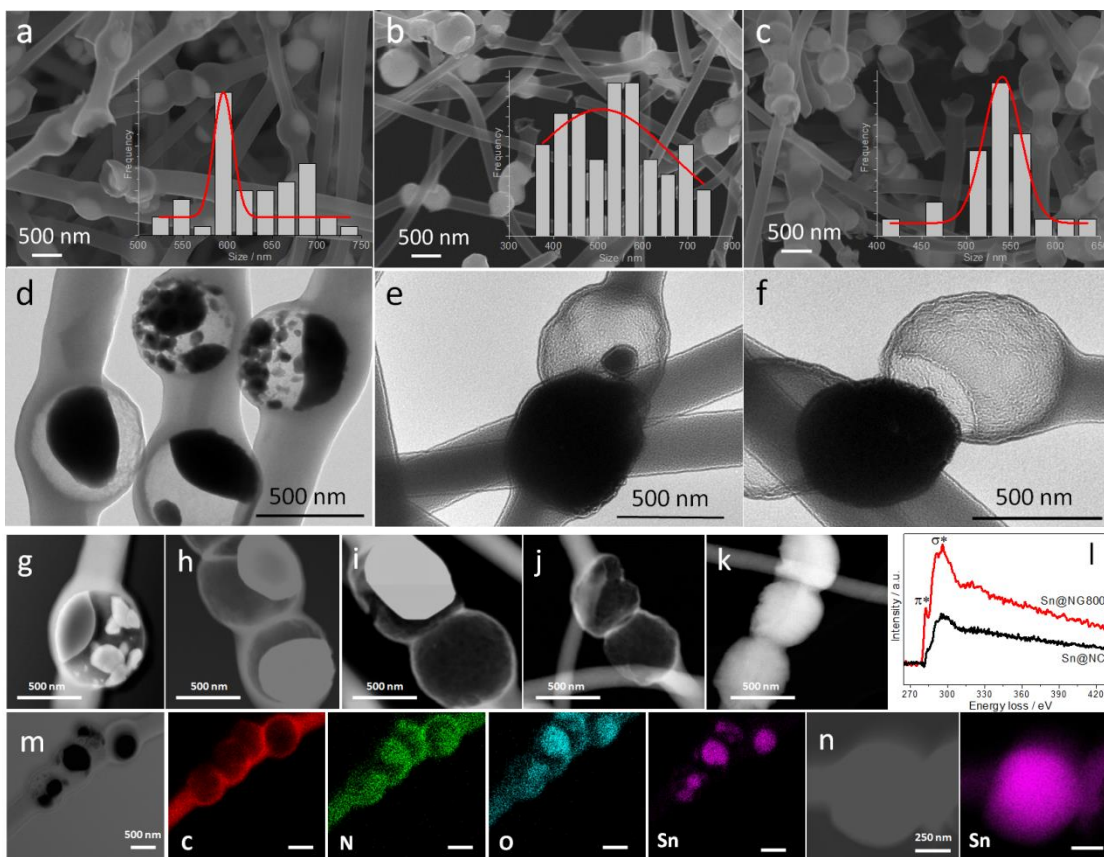


Figure 2 Electron microscopy. SEM and TEM images of (a, d) Sn@NC, (b, e) Sn@NG800 and (c, f) Sn@NG900. Inserts in the SEM images are size distributions of the spheres. HAADF-STEM images of (g) Sn@NC, (h, i) Sn@NG900, (j) hollow graphite spheres after Sn leakage in

Sn@NG900 and (k) Sn@NG800. (l) Carbon K-edge EELS of Sn@NC and Sn@NG800. EDX elemental mapping of carbon, nitrogen, oxygen and tin in (m) Sn@NC and (n) Sn@NG800.

Table 1 Quantification of chemical bonds between C and N in the samples.

Sample	Pyridinic N (N5)	Pyrrolic N (N6)	Graphitic N
Sn@NC	50.2%	22.9%	26.9%
Sn@NG800	21.8%	43.6%	34.6%
Sn@NG900	26.1%	33.5%	40.4%

SEM images of Sn@NC, Sn@NG800 and Sn@NG900 are shown in Figure 2a-c with insets plotting the size distribution of the spheres on the carbon nanofibers. The high electron accelerating voltage of 20 kV in the SEM allows a large interaction volume with samples to display topographical characteristics below the surface, and the SEM images show clear contrast between carbon and Sn of different atomic weight, resulting from the detection of more backscattered electrons. Transmission Electron Microscopy (TEM) images in Figure 2(d-f) and high-angular annular dark-field scanning TEM (HAADF-STEM) images in Figure 2(g-k) indicate that the spherical structures of Sn@NC and Sn@NG900 are yolk-shell while Sn@NG800 is core-shell with tight cohesion between the Sn core and NG shell. Energy-dispersive X-ray spectroscopy (EDX) elemental mappings of Sn@NC (Figure 2m) and Sn@NG800 (Figure 2n) indicate that the core and yolk parts are Sn, and that the shell of Sn@NC is nitrogen-doped carbon with a high amount of oxygen, consistent with the XPS results.

The structural evolution of the spheres was studied by TEM and HAADF-STEM. Figures 2(d, g) show that the yolk parts in the spheres of Sn@NC are nano Sn fragments, resulting from the thermal vapor removal of Zn from ZnSn(OH)<sub>6</sub> at 800 °C. An increase in the temperature to 900 °C melts the Sn fragments into one large block in Sn@NG900, see Figures 2(f, h). Sn@NG900 displays voids between the yolk blocks and NG shells, and apertures on the shell (Figure S7) resulting from the cohesive force of liquid Sn and high-temperature pyrolysis. Once the shell apertures are large enough, the tin blocks leak out (Figure 2f) leaving hollow NG shells (Figure 2j) or merge with another block in an adjacent shell (Figure 2i). This process causes Sn loss in the whole nanofiber and leads to a relatively high carbon content (47.8%) compared with Sn@NG800. At a temperature of 800 °C fusing the nano fragments occurs, keeping the Sn particles in the fiber structure for pyrolysis times up to 5h. Figures 2e and S8 show that Sn@NG800 has a well-defined core-shell Sn@C structure, resulting from the strain of liquid Sn and extending pyrolysis. Scheme 1 represents the structural evolution during thermal vapor of Zn and melting of Sn from: (I) ZnSn(OH)<sub>6</sub>@PAN fibers to (II) Sn fragments@NC, (III) Sn block@NG and (IV) hollow NG in a single sphere (Scheme 1a) and interconnected double spheres (Scheme 1b). The Gaussian-fitted size distributions in the insets of Figure 2(a-c) reveal that the mean size of the spheres in Sn@NC, Sn@NG800 and Sn@NG900 are 595, 506 and 537 nm. The size decreases when the Sn fragments are fused into blocks and the shells become graphitized. The tuning of the sphere size is highly dependent on the toughness of the shells under the strains of liquid Sn. The shells of core-shell Sn@NG800 have a large shrinkage of 15% compared to those of Sn@NC (Figure 2k) and yolk-shell Sn@NG900 shows apertures and voids on the shell with a shrinkage of 9.7%. The leakage of Sn liquid in the pyrolysis and the specifically produced NG shell of Sn@NG900 lead to the yolk-shell structure. The different

properties of the carbon shells in Sn@NC and NG shells in Sn@NG800 are characterized by electron energy loss spectroscopy (EELS) and the resulted carbon K-edge spectra are displayed in Figure 2i. The features are typical for carbon materials and represent the energy state with  $\pi$  or  $\sigma$  symmetry, where the peak at 282.5 eV denotes  $1s \rightarrow \pi^*$  transition and the higher loss energy ( $>295$  eV) is due to  $1s \rightarrow \sigma^*$  transition, corresponding to the  $sp^2$ - and  $sp^3$ - hybridized carbons<sup>31</sup>, respectively. The well-identified peaks in Sn@NG800 indicate a mixed hybridization of carbons, which is similar to graphite. Sn@NC shows a weak  $\pi^*$  peak and a rounded  $\sigma^*$  peak followed by a shallow slope, which is typical for amorphous carbon, indicating insignificant graphitization of PAN and a high amount of amorphous state in the shell<sup>32</sup>. Amorphous carbon is brittle and can sustain little deformation while graphite, as a crystalline carbon material has high strength and toughness<sup>33</sup>. The formed NG shells in Sn@NG800 possess higher graphitization than that of Sn@NG900 and Sn@NC.

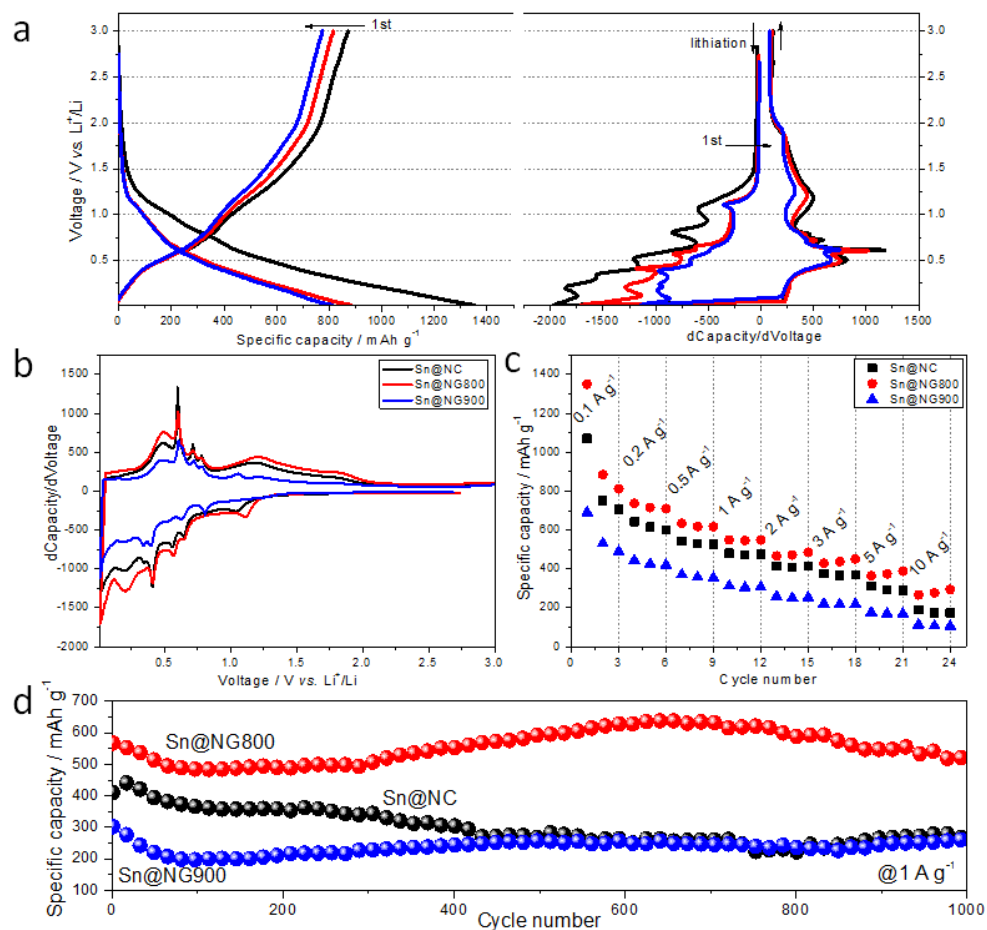
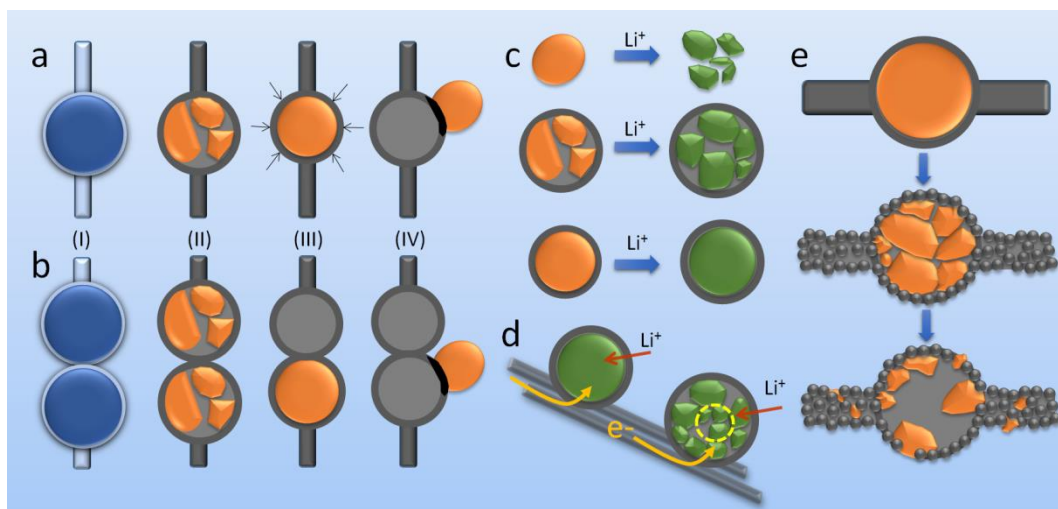


Figure 3 Electrochemical characterization. (a) Galvanostatic charge-discharge profiles of Sn@NG800 at 0.1 A g<sup>-1</sup> in the first three cycles and the corresponding differential capacity (dQ/dV) curves. (b) Differential capacity curves of Sn@NC, Sn@NG800 and Sn@NG900 from the charge-discharge current of 0.1 A g<sup>-1</sup>. (c) Rate performance at current rates from 0.1 to 10 A g<sup>-1</sup> and (d) cycling performance at 1 A g<sup>-1</sup> of Sn@NC, Sn@NG800 and Sn@NG900.



Scheme 1 Step-wise thermal vapor and melting process from (I)  $\text{ZnSn}(\text{OH})_6@\text{PAN}$  to (II) Sn fragments@NC, (III) Sn block@NG and (IV) hollow NG in (a) single spherical structure and (b) double or multiple spheres. (c) Lithiation in specific structures of Sn particle, Sn fragments@NC and Sn block@NG (from top to bottom). (d) Schematic illustration of the conduction of electrons and lithium ions in Sn@C sphere-chain structures. The discontinuous contact between Sn fragments leaves limited area with poor electron and ionic conduction. (e) Proposed structure evolution of the Sn@NG800 in the cycling lithiation/de-lithiation process. Sn core gradually pulverizes into small particles and the NG shell becomes amorphous with disordered pores on the surface and in the fibers. Sn particles are embedded into the carbon nanofibers by surface adsorption or inner diffusion along the fibers.

The obtained Sn-C hybrid samples are used as anode materials in lithium-ion batteries working in a voltage window of 0.01~3 V and their electrochemical performance is displayed in Figure 3. Galvanostatic charge-discharge profiles of Sn@NG800 at 0.1 A  $\text{g}^{-1}$  in Figure 3a shows the initial reversible capacity is 872 mAh  $\text{g}^{-1}$  which arises from the Sn alloying with lithium ions ( $\text{Sn} + x\text{Li} + xe^{-1} \rightarrow \text{Li}_x\text{Sn}$ ,  $0 \leq x \leq 4.4$ )<sup>9</sup> and lithium intercalation into the graphite shell, with a

coulombic efficiency of 65%. The pyrolysed PAN has been reported with a low specific capacity (100~300 mAh g<sup>-1</sup>)<sup>20, 34, 35</sup> in the lithium storage. For better comparison, the pyrolysed PAN-5h nanofibers were tested and the specific capacity is 288 mAh g<sup>-1</sup> at 0.1 A g<sup>-1</sup> (Figure S9) contributing to less than 10% of the whole capacity of Sn@NG800 based on the carbon content. The irreversible capacity in the first cycle is due to the formation of solid electrolyte interphase (SEI) film and/or lithiation in the vicinity of residual H atoms in the carbon materials<sup>36</sup>. The following two cycles of Sn@NG800 have a capacity of 884 and 811 mAh g<sup>-1</sup> with rising coulombic efficiency of 92.3% and 95.6%. This gradual increase in coulombic efficiency is typical for carbon-based materials and indicates the nearly saturated consumption of lithium ions by electrolyte decomposition and residual active groups on the carbon surface<sup>37</sup>. Differential capacity analysis (dQ/dV) of Sn@NG800 is displayed in Figure 3a where the peaks in these curves indicate the voltages at which the majority of charges enter or leave the material. A peak at 0.8 V in the first lithiation reaction disappears in the subsequent cycles, suggesting the voltage of electrolyte decomposition and SEI layer formation. While the potential is 0.6 V for PAN-5h at 0.1 A g<sup>-1</sup> from the dQ/dV profiles plotted in Figure S10, and the difference is due to the variation in the electrode-electrolyte interface<sup>38</sup> arising from the nanosized Sn and surface state of the pyrolyzed carbon. The irreversible process of Sn@NG800 is also confirmed by the large and broad peak in the cyclic voltammetry profile of the first scan in Figure S11. The peaks located in the range of 0.4~0.8 V correspond to the alloying/dealloying reaction between Sn and lithium ions<sup>39</sup> and the peaks around 0.2 V originate from the reversible intercalation/deintercalation of lithium ions into/from carbon<sup>40</sup>, which are also observed in the dQ/dV profiles of PAN-5h in Figure S10. The first cathodic peak around 1 V is due to surface charge transfer through the small graphitic clusters to allow the lithium ions to pass and react with the inner Sn.

This capacitive redox behavior (pseudocapacitance) on the surface is evidenced by the linear increase in the currents at 1 V with the increasing scan rates (Figure S12), which is beneficial for the ion diffusion and high-rate performance. Figure 3b compares the differential capacity profiles of Sn@NC, Sn@NG800 and Sn@NG900 at a current of 0.1 A g<sup>-1</sup>. The lithiation potentials of Sn and graphite are similar in these three samples but their surface redox potentials are different. The surface redox arises from lithium intercalation and the lower potential for Sn@NG900 results from the suspended Sn particles and hollow NG spheres leading to a mixed redox behavior on their surface, in comparison with Sn@NG800 and Sn@NC which possess hierarchical core- and yolk-shell structures.

Figure 3c displays the specific capacities of the samples at various current rates from 0.1 to 10 A g<sup>-1</sup>, and Figure 3d plots their long-term cycling stability, with Sn@NG800 showing the best. The average capacities at 0.1, 0.2, 0.5, 1, 2, 3, 5, 10 A g<sup>-1</sup>, of Sn@NG800 are 884, 715, 619, 545, 472, 438, 374, 278 mAh g<sup>-1</sup>, larger than Sn@NC, 750, 615, 530, 472, 409, 368, 291, 174 mAh g<sup>-1</sup> and Sn@NG900, 531, 426, 357, 306, 251, 217, 170, 107 mAh g<sup>-1</sup>. Both Sn@NC and Sn@NG900 have a large content of pyrolysed PAN or residues, resulting in a low specific capacity. The cycling profiles of Sn@NG800 display a drop-increase-drop fluctuation in the capacity, with a high capacity retention of 91.8% after 1000 cycles at a large current of 1 A g<sup>-1</sup>. The capacity drop is due to the material fading and the increase may be ascribed to the electrode activation<sup>41</sup> allowing high-area access by the electrolyte. The capacity retention of Sn@NG900 is 88.3% and Sn@NC is 65%. The high stability of Sn@NG800 is due to the NG shell. On one hand, the shell with enriched porosity and surface area can buffer the volume change of Sn; on the other hand, the content of pyridinic N atoms, which prefer to bond at the edges or defects of the carbon materials and cause high resistance,<sup>42</sup> is not too high in the shell. Scheme 1c depicts

the lithiation in a Sn particle, Sn fragments@NG and Sn block@NG (from top to bottom). The alloying reaction causes cracks and pulverization of the Sn electrode, resulting in the breakdown of electric conduction pathways between the electrode and current collector, leading to fast capacity fade, and poor lifespan and rate performance. The yolk-shell framework allows the Sn pulverization inside the limited area of the shell during alloying, maintaining the contact with the current collector, but as shown in Scheme 1d, the nearly dangling Sn fragments in the center of the sphere have poor contact with other Sn particles and the carbon matrix resulting in poor access by both electrons and ions, lowering capacity. The core-shell structure has better binding between the Sn and NG shell, ensuring the fast electron and ion conduction and leading to improved performance, in good agreement with the previous work<sup>43</sup>. To clarify the promising performance of the as-prepared materials used for lithium battery storage, the difference is compared to Sn-based materials in Table 2. The specific capacity of Sn@NG800 is comparable with the literature although extremely high values have been achieved for specific composite materials with Sn, such as reduced graphene oxide<sup>44</sup>. Sn@NG800 shows ultrasmall degradation in the specific capacity per cycle compared to the reported results, indicating the high cycling stability.

Table 2 Comparison with publications of Sn-based anode materials in specific capacity and cycling stability.

Materials	Specific capacity/mAh g <sup>-1</sup>	Degradation per cycle
Sn nanoparticles <sup>41</sup>	450@0.99A g <sup>-1</sup>	0.44%@0.1A g <sup>-1</sup>
Sn nanocrystals <sup>9</sup>	750@0.99A g <sup>-1</sup>	0.31%@0.1A g <sup>-1</sup>
Sn-carbon core-shell powder <sup>39</sup>	424@0.04A g <sup>-1</sup>	0.78%@0.04A g <sup>-1</sup>

Sn-rGO <sup>45</sup>	793@0.05A g <sup>-1</sup>	0.46%@0.05A g <sup>-1</sup>
Sn-Co-graphite composite <sup>46</sup>	556@0.05A g <sup>-1</sup>	0.53%@0.05A g <sup>-1</sup>
Porous Sn@Carbon <sup>47</sup>	672@0.025A g <sup>-1</sup>	0.016%@0.025A g <sup>-1</sup>
Graphene-Sn@CNT <sup>48</sup>	828@1A g <sup>-1</sup>	0.15%@0.1A g <sup>-1</sup>
Graphene-Sn nanosheets <sup>49</sup>	800@0.05A g <sup>-1</sup>	0.44%@0.05A g <sup>-1</sup>
RGO-Sn nanocables <sup>44</sup>	1572@0.1A g <sup>-1</sup>	1.2%@0.1A g <sup>-1</sup>
Mesoporous Sn/C <sup>50</sup>	510@1A g <sup>-1</sup>	0.15%@0.5A g <sup>-1</sup>
Sn@NG800 (this work)	884@0.1A g <sup>-1</sup>	0.0082%@1A g <sup>-1</sup>

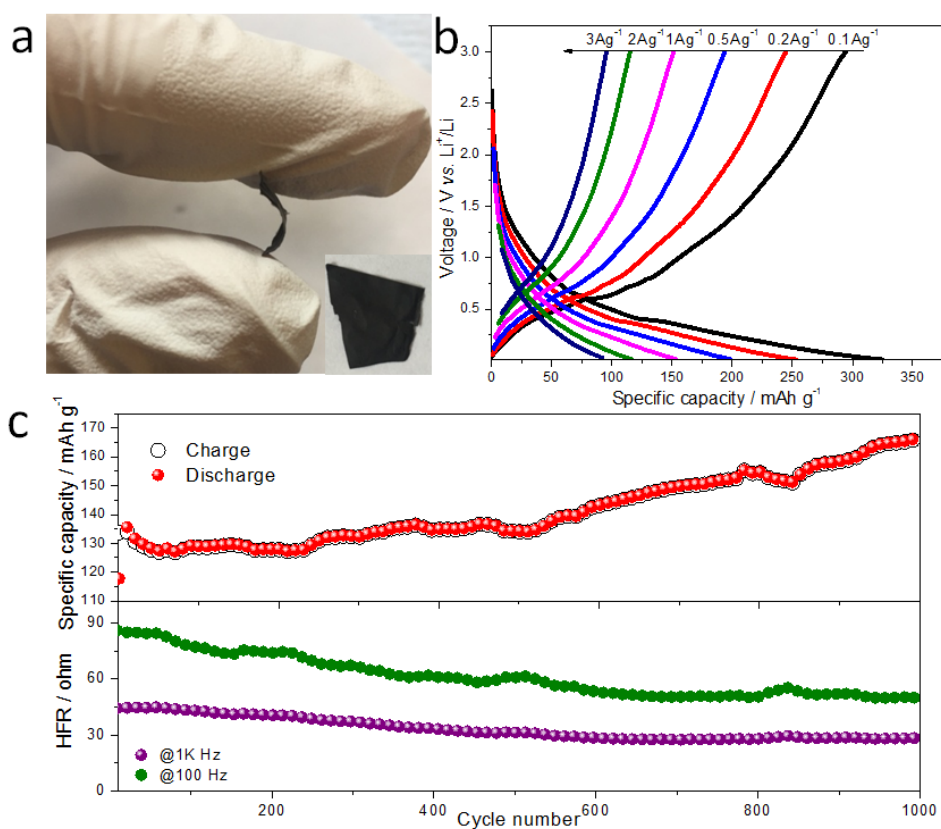


Figure 4 Suspended sheet of Sn@NG800 as an anode for lithium storage. (a) Pictures of the sample and its flexibility. (b) Galvanostatic charge-discharge profiles at different current rates.

(c) Cycling performance at a current of  $1 \text{ A g}^{-1}$  with corresponding in-situ high-frequency resistance at 1 kHz and 100 Hz.

The sheets obtained from the pyrolysis of  $\text{ZnSn}(\text{OH})_6@\text{PAN}$  fibers have high flexibility as shown in Figure 4a. A piece of  $\text{Sn}@\text{NG800}$  sheet has been directly used as the anode material in lithium-ion batteries without extra binder and conductive agent. Figure 4b shows the charge-discharge profiles of the suspended  $\text{Sn}@\text{NG800}$  electrode at current rates of 0.1, 0.2, 0.5, 1, 2 and  $3 \text{ A g}^{-1}$ , corresponding to specific capacities of 325, 253, 199, 153, 111 and  $92 \text{ mAh g}^{-1}$ . These capacities are much lower than the electrodes mixed with binder and conductive carbon, resulting from the loose and low-density fibers with poor contact with each other and the electrolyte. The cycling performance of the suspended electrode at  $1 \text{ A g}^{-1}$  in Figure 4c displays a rise in the specific capacity by 22% after 1000 cycles from the beginning  $136 \text{ mAh g}^{-1}$  with high coulombic efficiency close to 100%. The capacity increase is due to the electrochemical activation and stabilization of these electrode materials<sup>51</sup> of loose nanofibers. Moreover, the low-potential operation causes reversible formation of organic polymeric/gel-like layer by electrolyte decomposition which is capable of coating around the active materials to improve the mechanical cohesion and deliver extra capacity through a so-called pseudo-capacitance-type behavior<sup>52</sup>. The cohesion enhancement combines the separate nanofibers into a network that improves the transport of both electrons and lithium ions. Figure 4c shows the *in-situ* high frequency resistance (HFR) of the electrode in cycling at 1 kHz and 100 Hz. Both values drop gradually with cycling due to the structure optimization of the electrode materials. The suspended  $\text{Sn}@\text{NG800}$  sheet electrode offers great potential to investigate structural evolution in cycling, by avoiding the influence from binder and conductive agents.

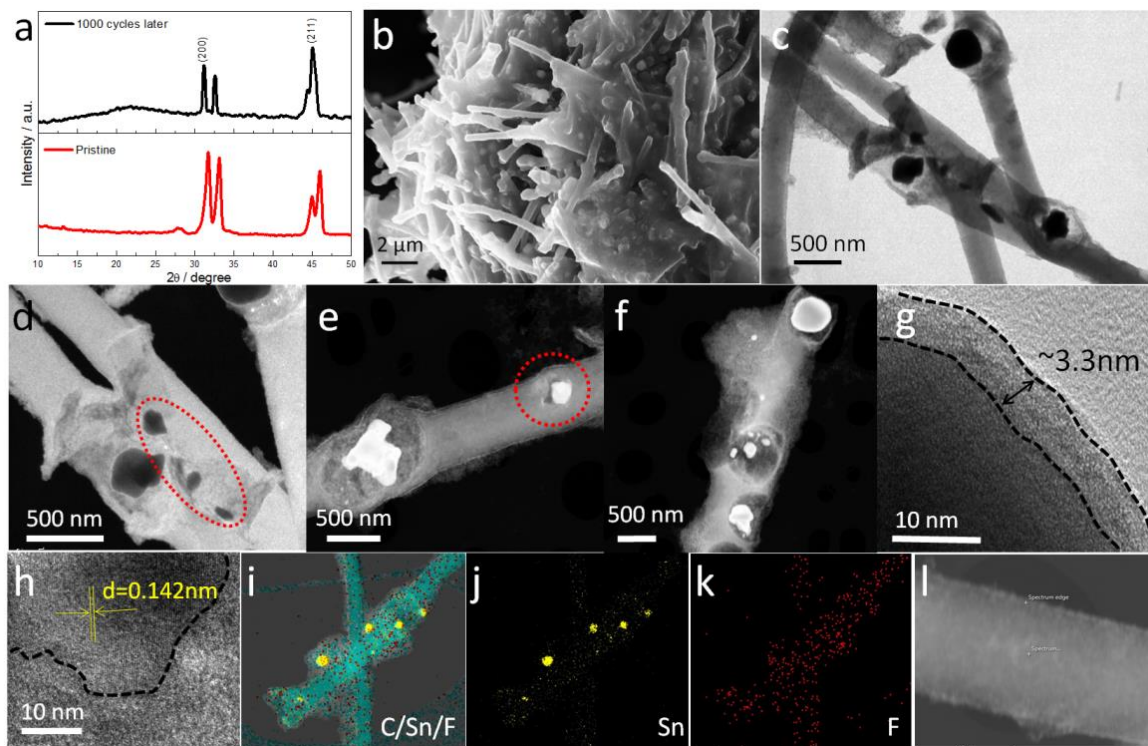


Figure 5 Material characterization of the suspended Sn@NG800 sheet electrode after 1000 cycles. (a) XRD patterns. (b) SEM images. (c) TEM images. (d) Dark-field TEM image. (e, f) STEM image. (g, h) High-resolution TEM image. EDX mapping images of (i) mixed elements C (blue), Sn (yellow), and F (red), (j) Sn, (k) F. (l) STEM image of a carbon fiber for EDX. One spectrum is picked up from the edge and another is from the center.

Figure 5 displays the characterization results of the suspended Sn@NG800 sheet electrode after 1000 cycles. The XRD patterns in Figure 5a shows that the main peaks of Sn@NG800 after cycling shift to low angles, and that the domain size along (200) increases to 60.7 nm, implying the potential nucleation and growth of Sn crystals along (200) in the phase transition<sup>53</sup>. The relative intensity of (211) peak grows after the cyclic lithiation/de-lithiation reaction of Sn, indicating that the (211) planes are preferred in the reaction and their surface energy has been tuned lower during cycling. The robust pattern of graphite in Sn@NG800 has disappeared after

cycling and the broad peak around  $20^\circ$  denotes the amorphous state of carbon resulting from the disordering destruction of the graphitic carbon by the continuous lithiation/de-lithiation. The SEM image in Figure 5b displays the agglomerated fibers in the polymeric layers with beneficial mechanical cohesion and conduction of  $\text{Li}^+/\text{e}^-$  among these fibers. EDX in Figure S13 indicates that the polymeric layers contain fluorine and phosphorus, implying that they are originally from the decomposed electrolyte. The TEM image in Figure 5c shows well-maintained carbon nanofibers and spheres with inner tin particles and carbon shells. The electron diffraction patterns of the tin-containing spheres show polycrystallinity while the carbon nanofibers are amorphous, see Figure S14, in agreement with the post-cycling XRD results. After cycling, the tin cores in the starting  $\text{Sn}@NG800$  decrease the particle size from 500 nm to less than 260 nm but the small-size particles are still embedded into the carbon nanofibers, as observed in Figure 5 (d), the dark-field TEM image and Figure 5(e, f), the STEM images. The STEM image in Figure 5f displays the pores on the sphere shells that allow the small tin particles to flow out to embed into the carbon nanofiber (also see Figure S15) whilst some of the remaining Sn embeds into the inside carbon shell. Figure 5g shows a layer of SEI film with a thickness of around 3.3 nm on the surface of Sn particles. Tin remains highly crystalline and shows clear lattice planes of (321) with an interplanar distance of 0.142 nm in the high-resolution TEM (Figure 5h). The overlay EDX mapping of C, Sn and F in Figure 5i indicates the wide distribution of Sn in the carbon nanofibers and F on the surface of both Sn and carbon. The elemental mapping of Sn in Figure 5j denotes there are many Sn clusters along the fiber structure and F has a uniform distribution along the nanofibers (Figure 5k). To verify the content of the embedded tin clusters in the carbon nanofibers, EDX was performed on the edge and center of a fiber shown in Figure 5l. The EDX spectra and ratios of these detected elements are displayed in Figure S16 and Table S1, the

atomic ratio of tin in the center is 0.9% and at the edge is 3.4%. The different contents of Sn along the carbon nanofibers indicate the embedding is not uniform but dependent upon the porosity of the fibers. The structural characterizations of Sn@NG800 before and post the long-term cycling indicate a potential mechanism about how the structure evolves in the electrochemical cycling shown in Scheme 1e. On cycling, lithiation/de-lithiation causes the graphitic shells and fibers to be amorphous with disordered pores, and the small Sn particles that arise from the core pulverization can be embedded into the porous matrix through surface adsorption or diffusion along the nanofibers. The superior core-shell spheres interconnected by carbon nanofibers gives rise to a structural evolution that maintains the Sn@C structure during cycling, leading to high lithium-storage performance.

## Conclusions

Yolk-shell and core-shell Sn@C spheres interconnected by carbon nanofibers were synthesized by thermal vapor and thermal melting of electrospun fibers of ZnSn(OH)<sub>6</sub>@PAN, with tunable graphitization of the carbon shells. Sn inside the spheres possesses a dynamic structure evolution during thermal melting by fusing small particles into one block. The high graphitization of carbon nanofibers and intact Sn cores allow core-shell Sn@NG800 to perform the best in lithium storage, with 884 mAh g<sup>-1</sup> at 0.1 A g<sup>-1</sup> and a high capacity retention of 91.8% after 1000 cycles at a large current of 1 A g<sup>-1</sup>. The suspended sheet electrode shows increasing capacity but decreased resistance with cycling, and the changes in material structures post cycling prove that the pulverized tin particles have embedded into the disordered carbon nanofibers during cycling to maintain a Sn@C configuration. The superior core-shell spheres interconnected by carbon nanofibers provide a pathway in structural evolution to sustain a Sn@C structure in the electrochemical reaction, thus maintaining high lithium-storage performance.

## Experimental

**Material Synthesis:** The preparation of  $\text{ZnSn}(\text{OH})_6$  cubes follows the published method<sup>16</sup>. In brief,  $\text{SnCl}_4 \cdot 5\text{H}_2\text{O}$  (3.5g, 10mmol, from Sigma-Aldrich) was added into 50 mL ethanol under stirring for 10 minutes.  $\text{Zn}(\text{CH}_3\text{COO})_2 \cdot 2\text{H}_2\text{O}$  (2.2g, 10mmol, from Sigma-Aldrich) and sodium dodecyl sulphate (3.5g, 10mmol) were stirred in 100 mL distilled water for 10 minutes. The two solutions were then mixed and stirred for another 5 minutes followed by the addition of 50 mL NaOH solution (2M in water, NaOH is from Sigma-Aldrich). After stirring for overnight, the white products were collected by centrifuge and washed using distilled water, then dried in the oven at 60 °C in the air.

The as-prepared  $\text{ZnSn}(\text{OH})_6$  cubes (0.3g) were mixed with 0.3g polyacrylonitrile (PAN) powder (Goodfellow Cambridge Limited Huntingdon, mean particle size 50  $\mu\text{m}$ , mean molecular weight 230,000  $\text{g mol}^{-1}$ ) in 3 ml dimethylformamide (DMF, VWR chemicals, 99.90%) to prepare the electrospinning precursor. The precursor solution was filled into a syringe and driven into the electrospinning needle (13 mm length, flat-tipped, 0.41 mm inside diameter, 0.71 mm outside diameter) by a syringe pump (Graesby 3300) at 0.75  $\text{ml h}^{-1}$ . The needle was held at 13 kV using a high voltage power supply (GenVolt 73,030) a distance of 20 cm from the 20  $\times$  20 cm polished aluminium collector plate. Fibers were collected after 1 h of spinning (25 °C, 50% of humidity) from the collector plate. The fibers were pre-carbonized at 290 °C in air with a temperature increase rate 5 °C  $\text{min}^{-1}$  for 2 h, followed with further annealing at 800 and 900 °C in Ar at 5 °C  $\text{min}^{-1}$  for a specific time (2h or 5h) to obtain final sheet materials.

**Material Characterization:** The crystallographic structures of the as-prepared materials were studied by X-ray powder diffraction (XRD) using a Bruker D8 diffractometer with

monochromatic Cu K $\alpha$  radiation ( $\lambda=1.5406 \text{ \AA}$ ). Scanning electron microscopy (SEM) images were recorded on an LEO Gemini 1525 FEG. Transmission electron microscopy (TEM) images, selected area electron diffraction (SAED), scanning transmission electron microscopy (STEM) images, electron energy loss spectroscopy (EELS) with an energy resolution of about 1 eV were carried out on JEM 2100F with an operation voltage of 200 kV. Energy dispersive X-ray spectroscopy (EDX) was performed on a LEO Gemini 1525 FEG and JEM 2100F. X-ray photoelectron spectroscopy (XPS) was measured using a Thermo Scientific K-Alpha instrument. The thermogravimetric analysis/differential scanning calorimetry (TGA/DSC) of the samples was carried out on a Diamond TG thermo-analyzer. Raman spectroscopy and mapping were performed on a Renisha winVia with 50 $\times$  objective and 514nm laser as excitation source.

**Electrochemical tests:** The as-prepared electrode materials were mixed with acetylene black and binder (sodium carboxymethyl cellulose, CMC) in a weight ratio of 7:2:1 using distilled water as solvent. The slurry was placed on a copper foil as current collector and the electrode was dried in a vacuum oven at 80  $^{\circ}\text{C}$  for 24 h. The gravimetric density of the used electrode materials is close to 1 mg cm $^{-2}$ . R2032 coin cells were assembled in an argon-filled glove box using metallic lithium as the cathode and a Celgard 2500 membrane as separator. The electrolyte was 1 M LiPF $_6$  dissolved in a mixture of ethylene carbonate (EC) and dimethyl carbonate (DMC) (v/v, 1/1). The suspended electrode sheet was cut into specific area and directly assembled in the coin cell without the use of binder and conductive agent. Cyclic voltammetry (CV) and galvanostatic charge/discharge cycling tests were carried out over a set voltage range using an Autolab workstation (GPES software) and a 580 Bycycle battery test system, respectively. All electrochemical tests were carried out at room temperature.

## ASSOCIATED CONTENT

**Supporting Information.** More results of material characterization and electrochemical measurement.

## ACKNOWLEDGMENT

We thank the President's Ph.D. Scholarship of Imperial College London, the Engineering and Physical Sciences Research Council (EPSRC, Grant: EP/L015277/1), Armourers & Brasiers Rolls-Royce Scheme Award (2018) and STFC Futures Early Career Award (2016) for financial support. The Authors acknowledge use of characterisation facilities within the Harvey Flower Electron Microscopy Suite and the use of facilities in Ainara Aguadero's lab, Department of Materials, Imperial College London.

## REFERENCES

1. A. Manthiram, *ACS Cent Sci*, 2017, **3**, 1063-1069.
2. D. Da, *Energy Sci Eng*, 2015, **3**, 385-418.
3. S. Wu, R. Xu, M. Lu, R. Ge, J. Iocozzia, C. Han, B. Jiang and Z. Lin, *Adv Energy Mater*, 2015, **5**, 1500400.
4. Y. Lu, L. Yu and X. W. Lou, *Chem*, 2018, **4**, 972-996.
5. L. Liu, F. Xie, J. Lyu, T. Zhao, T. Li and B. G. Choi, *J Power Sources*, 2016, **321**, 11-35.
6. Y. Idota, T. Kubota, A. Matsufuji, Y. Maekawa and T. Miyasaka, *Science*, 1997, **276**, 1395-1397.
7. Y. Hangjun and H. Wei-Qiang, *Adv Sci*, 2017, **4**, 1700298.
8. K. D. Kepler, J. T. Vaughey and M. M. Thackeray, *J Power Sources*, 1999, **81-82**, 383-387.
9. H. S. Im, Y. J. Cho, Y. R. Lim, C. S. Jung, D. M. Jang, J. Park, F. Shojaei and H. S. Kang, *ACS Nano*, 2013, **7**, 11103-11111.
10. N. Zhang, Q. Zhao, X. Han, J. Yang and J. Chen, *Nanoscale*, 2014, **6**, 2827-2832.
11. Y. Xu, Q. Liu, Y. Zhu, Y. Liu, A. Langrock, M. R. Zachariah and C. Wang, *Nano Lett*, 2013, **13**, 470-474.
12. Y. Yu, L. Gu, C. Zhu, P. A. van Aken and J. Maier, *J Am Chem Soc*, 2009, **131**, 15984-15985.
13. Y. Yan, G. Lin, W. Chunlei, D. Abirami, v. A. P. A. and M. Joachim, *Angew. Chem. Int. Ed.*, 2009, **48**, 6485-6489.
14. L. Yongchang, Z. Ning, J. Lifang and C. Jun, *Adv Mater*, 2015, **27**, 6702-6707.
15. Z. Hongwei, H. Xiaodan, N. Owen, Z. Liang and Y. Chengzhong, *Adv Funct Mater*, 2017, **27**, 1606023.
16. L. Sun, X. Han, Z. Jiang, T. Ye, R. Li, X. Zhao and X. Han, *Nanoscale*, 2016, **8**, 12858-12862.
17. W. Song, K. Ji, A. Aguadero, P. R. Shearing, D. J. L. Brett, F. Xie and D. J. Riley, *Energy Storage Materials*, 2018, **14**, 324-334.

18. M. Thakur, S. L. Sinsabaugh, M. J. Isaacson, M. S. Wong and S. L. Biswal, *Sci Rep*, 2012, **2**, 795.
19. F. M. Hassan, R. Batmaz, J. Li, X. Wang, X. Xiao, A. Yu and Z. Chen, *Nat Commun*, 2015, **6**, 8597.
20. W.-S. Chang, C.-M. Park and H.-J. Sohn, *J Electroanal Chem*, 2012, **671**, 67-72.
21. Q.-Y. Chen, L. Liu and Y.-H. Wang, *ADV COND MATTER PHYS*, 2014, **2014**, 5.
22. X. Zhang, L. Ji, O. Toprakci, Y. Liang and M. Alcoutlabi, *Polym Rev*, 2011, **51**, 239-264.
23. H. Hou, C. E. Banks, M. Jing, Y. Zhang and X. Ji, *Adv Mater*, 2015, **27**, 7861-7866.
24. H. Hongshuai, S. Lidong, Z. Yan, Z. Guoqiang, C. Jun and J. Xiaobo, *Adv Sci*, 2017, **4**, 1600243.
25. W. Song, J. Lischner, V. G. Rocha, H. Qin, J. Qi, J. H. L. Hadden, C. Mattevi, F. Xie and D. J. Riley, *ACS Energy Letters*, 2017, **2**, 1144-1149.
26. J. Zhao, Y. Liu, X. Quan, S. Chen, H. Yu and H. Zhao, *Appl Surf Sci*, 2017, **396**, 986-993.
27. Y. Xu, C. Zhang, M. Zhou, Q. Fu, C. Zhao, M. Wu and Y. Lei, *Nat Commun*, 2018, **9**, 1720.
28. H. Wang, N. Yang, W. Li, W. Ding, K. Chen, J. Li, L. Li, J. Wang, J. Jiang, F. Jia and Z. Wei, *ACS Energy Letters*, 2018, **3**, 1345-1352.
29. H. Yuan, W. Zhang, J.-g. Wang, G. Zhou, Z. Zhuang, J. Luo, H. Huang, Y. Gan, C. Liang, Y. Xia, J. Zhang and X. Tao, *Energy Storage Materials*, 2018, **10**, 1-9.
30. F. Zheng, Y. Yang and Q. Chen, *Nat Commun*, 2014, **5**, 5261.
31. V. V. Roddatis, V. L. Kuznetsov, Y. V. Butenko, D. S. Su and R. Schlögl, *Phys Chem Chem Phys*, 2002, **4**, 1964-1967.
32. J. W. Moreau and T. G. Sharp, *Astrobiology*, 2004, **4**, 196-210.
33. W. Yang, S. Mao, J. Yang, T. Shang, H. Song, J. Mabon, W. Swiech, J. R. Vance, Z. Yue, S. J. Dillon, H. Xu and B. Xu, *Sci Rep*, 2016, **6**, 24187.
34. J. K. Lee, K. W. An, J. B. Ju, B. W. Cho, W. I. Cho, D. Park and K. S. Yun, *Carbon*, 2001, **39**, 1299-1305.
35. M. H. Kjell, E. Jacques, D. Zenkert, M. Behm and G. Lindbergh, *J Electrochem Soc*, 2011, **158**, A1455-A1460.
36. L. Qie, W. M. Chen, Z. H. Wang, Q. G. Shao, X. Li, L. X. Yuan, X. L. Hu, W. X. Zhang and Y. H. Huang, *Adv Mater*, 2012, **24**, 2047-2050.
37. B. Duan, W. Wang, H. Zhao, B. Xu, K. Yuan and Y. Yang, *J Electrochem Soc*, 2012, **159**, A2092-A2095.
38. M. Gauthier, T. J. Carney, A. Grimaud, L. Giordano, N. Pour, H.-H. Chang, D. P. Fenning, S. F. Lux, O. Paschos, C. Bauer, F. Maglia, S. Lupart, P. Lamp and Y. Shao-Horn, *The Journal of Physical Chemistry Letters*, 2015, **6**, 4653-4672.
39. Y. S. Jung, K. T. Lee, J. H. Ryu, D. Im and S. M. Oh, *J Electrochem Soc*, 2005, **152**, A1452-A1457.
40. B. Xu, L. Shi, X. Guo, L. Peng, Z. Wang, S. Chen, G. Cao, F. Wu and Y. Yang, *Electrochim Acta*, 2011, **56**, 6464-6468.
41. S. Xun, X. Song, V. Battaglia and G. Liu, *J Electrochem Soc*, 2013, **160**, A849-A855.
42. Q. Lv, W. Si, J. He, L. Sun, C. Zhang, N. Wang, Z. Yang, X. Li, X. Wang, W. Deng, Y. Long, C. Huang and Y. Li, *Nat Commun*, 2018, **9**, 3376.
43. A. Chojnacka, M. Molenda, D. Majda, P. Natkański and R. Dziembaj, *J Therm Anal Calorim*, 2017, **127**, 47-53.
44. L. Bin, W. Bin, L. Minghui, N. Jing, L. Xianglong and Z. Linjie, *Adv Mater*, 2012, **24**, 1405-1409.
45. C. Botas, D. Carriazo, G. Singh and T. Rojo, *J Mater Chem A*, 2015, **3**, 13402-13410.
46. T. Huang, Y. Yao, Z. Wei, Z. Liu and A. Yu, *Electrochim Acta*, 2010, **56**, 476-482.
47. L. Xifei, D. Abirami, G. Lin and W. Chunlei, *Adv Energy Mater*, 2012, **2**, 238-244.
48. Y. Zou and Y. Wang, *ACS Nano*, 2011, **5**, 8108-8114.
49. L. Bin, W. Bin, L. Xianglong, J. Yuying, L. Minghui and Z. Linjie, *Adv Mater*, 2012, **24**, 3538-3543.
50. J. Chen, L. Yang, S. Fang and S.-i. Hirano, *Electrochem. Commun.*, 2011, **13**, 848-851.
51. W.-J. Yu, P.-X. Hou, F. Li and C. Liu, *J Mater Chem*, 2012, **22**, 13756-13763.

52. Z. Wang, D. Luan, S. Madhavi, Y. Hu and X. W. Lou, *Energ Environ Sci*, 2012, **5**, 5252-5256.
53. H. Liu and C. P. Grey, *J Mater Chem A*, 2016, **4**, 6433-6446.